

Measurements of enriched ^{155}Gd and ^{157}Gd converters with the NMX detector on the n_TOF EAR2 beam line at CERN

D. Pfeiffer^{a,b,c} F.M. Brunbauer^b I.R. Fehse^{b,c} A.D. Finke^a K. Fissum^a K.J. Floethner^b D. Janssens^b M. Lisowska^b H. Muller^{b,f} E. Oksanen^a E. Oliveri^b L. Ropelewski^b A. Rusu^d J. Samarati^{a,b} L. Scharenberg^b M. van Stenis^b R. Veenhof^{b,e} N. Zavaritskaya^{b,f}

^a*European Spallation Source ESS ERIC (ESS),
Box 176, SE-221 00 Lund, Sweden*

^b*European Organization for Nuclear Research (CERN),
1211 Geneva 23, Switzerland*

^c*Friedrich-Abel-Gymnasium, Alter Postweg 6, 71665 Vaihingen Enz, Germany*

^d*SRS Technology, 30 Promenade des Artisans, 1217 Meyrin, Switzerland*

^e*Bursa Uludağ University,
Görükle Kampusu, 16059 Niüfer/Bursa, Turkey*

^f*Lycee International, Saint Genis-Pouilly, France*

E-mail: dorothea.pfeiffer@ess.eu

¹Corresponding author.

ABSTRACT: The detectors for the NMX instrument at the European Spallation Source (ESS) in Lund use natural Gd as the neutron converter. In 2024, beam time was obtained at the neutron time-of-flight experiment (n_TOF) at CERN to study the feasibility of an upgrade to enriched Gd. A $10 \times 10 \text{ cm}^2$ prototype of the NMX detector was equipped with two enriched Gd samples (^{157}Gd and ^{155}Gd) that were attached with copper tape to the natural Gd cathode of the detector. Three sets of measurements were taken, with the beam focused on either the natural Gd, the ^{157}Gd , or the ^{155}Gd samples. Using the time-of-flight technique with the subsequent conversion of time-of-flight into energy, the resonant region between 1 eV and 200 eV of the ^{157}Gd and ^{155}Gd cross sections was studied. The peaks in the resonant region were clearly visible, having higher ADC values in the ADC spectrum. Additionally, the resonant peaks had a larger number of counts per energy bin. In the thermal neutron energy range, the count rate at the center of the beam was measured for natural Gd, ^{157}Gd , and ^{155}Gd . Enriched ^{157}Gd showed an efficiency that was between 60 – 180 % higher, compared to natural Gd, for neutron wavelengths between 0.8 \AA and 1.8 \AA . The measured 60 % increase in efficiency at 1.8 \AA is lower than expected from simulations (100 %) and previous measurements with solid state detectors (80 %). Gamma background detection, bad focusing, and saturation effects most likely explain this deviation. An upgrade of the natural Gd converter to enriched ^{157}Gd would thus lead to an efficiency increase of at least 60 %. The measurements presented in this paper are the first successful time-of-flight measurements with the NMX detector prototype and the ESS VMM readout.

KEYWORDS: Neutron detectors (cold, thermal, fast neutrons), Neutron diffraction detectors, Gaseous detectors

Contents

1	Introduction	1
2	The NMX detector prototype	2
3	The experimental setup	3
4	The ESS readout system	4
5	Time-of-flight measurements	5
6	Comparison of the efficiencies of ^{157}Gd, ^{155}Gd and natural Gd	9
7	Conclusion	13

1 Introduction

The European Spallation Source (ESS) [1] in Lund, Sweden will become the world's most intense thermal neutron source with a significantly higher brilliance than at existing reactor or spallation sources. For the 15 neutron instruments that will comprise the initial instrument suite at ESS [2, 3], efficient thermal neutron detectors are a critical component [4]. The scientific user program for the first group of five instruments is expected to start in spring 2027. The macromolecular single-crystal diffractometer NMX [3] belongs to this first group, and requires three $51.2 \times 51.2 \text{ cm}^2$ detectors with at least reasonable detection efficiency (around 25% for cold neutrons in the center of the wavelength range from 1.8 to 10 \AA), sub-mm spatial resolution [5] and a good (0.1 ms) time resolution. The combination of solid neutron converters with micro pattern gaseous detectors (MPGDs) [6, 7] is a promising option to achieve these requirements. Currently, the NMX detector consists of a natural gadolinium neutron converter mounted as cathode in a triple GEM detector [8] with a low material budget x/y strip readout. Since beam time at ESS will be a precious commodity, it is paramount to optimize the neutron detection efficiency and the signal to background ratio of the neutron detectors. To improve the neutron detection efficiency, an upgrade of the natural gadolinium converter to an enriched ^{157}Gd converter is being considered. The relative improvement in detection efficiency of two samples of enriched ^{155}Gd and ^{157}Gd compared to natural gadolinium has been measured during two dedicated beam times at the EAR2 beamline of the n_TOF experiment at CERN. In 2024, 39 hours were allocated to us from March 20th to March 22nd and 17 hours from October 24th to October 25th.

2 The NMX detector prototype

For the measurements at n_TOF, a smaller $10 \times 10 \text{ cm}^2$ prototype was used in lieu of the full-size $51.2 \times 51.2 \text{ cm}^2$ detector (Figure 1a). The conversion volume (or drift space) is 10 mm long, and a $25 \mu\text{m}$ gadolinium foil serves as cathode and neutron converter. A drift field of 700 V/cm was chosen to avoid electron attachment to electronegative impurities and the subsequent loss of primary ionization electrons, while keeping the drift velocity smaller than $2.0 \text{ cm}/\mu\text{s}$ at atmospheric pressure. The three GEM foils [9] in the detector are mounted at a distance of 2 mm from each other and powered with a resistor chain. The values of the resistors are stated in Figure 1b. The detector operates at an effective gain of about 5000, and is usually flushed with Ar/CO_2 70/30 mixture at 5 l/h at room temperature and atmospheric pressure.

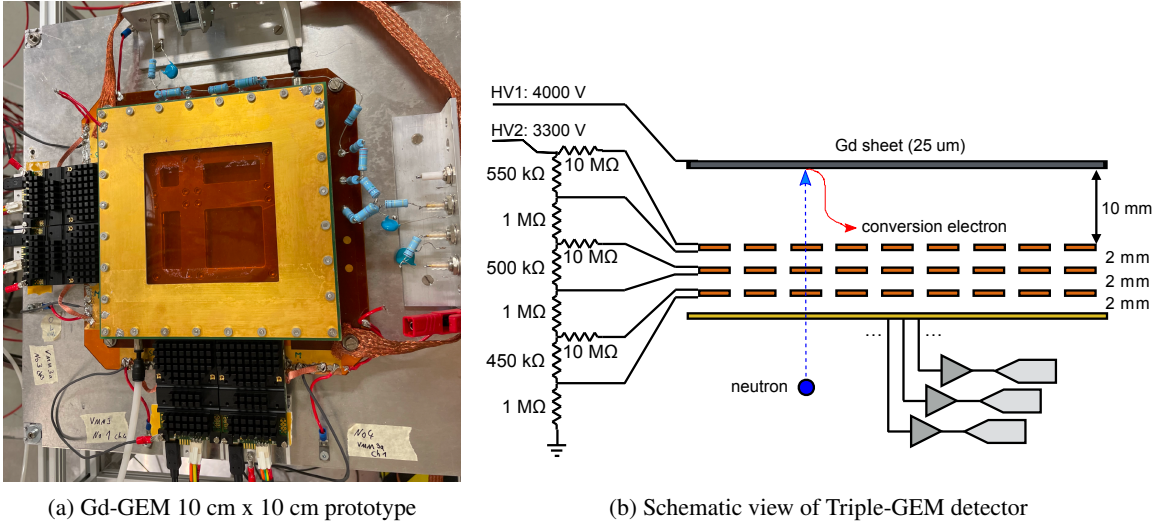


Figure 1. Gd-GEM neutron detector

A schematic drawing of the NMX detector is displayed in Figure 1b. The detector is operated in backwards mode. Neutrons traverse the low material budget detector readout and the three GEM foils, and then impinge on the natural Gd cathode. Natural Gd contains 14.8 % ^{155}Gd and 15.7 % ^{157}Gd . Both of these isotopes have a very high neutron capture cross section [10]. After the neutron capture, gadolinium releases prompt gamma particles with an energy of up to 9 MeV and conversion electrons with energies ranging from 29 keV to 250 keV. The signals resulting from these conversion electrons are used to determine the position of the neutron impact on the cathode with the help of the uTPC method [11, 12]. The strip pitch of the x/y readout is $400 \mu\text{m}$. There are 256 strips each in the x- and y-directions, which are read out with two RD51 VMM3a hybrids each in the x- and y-directions (figure 1a). Two VMM3a ASICs [13, 14] with 64 channels per chip are mounted on a RD51 VMM3a hybrid [15, 16], resulting in 128 channels per hybrid.

With this small prototype, a detection efficiency of 11.8% for neutrons with a wavelength of 2 \AA [12] was measured at IFE [17] in 2016. For that measurement, the detector used a traditional x/y strip readout that contained an FR4 base [18]. We replaced this with a low material budget readout that uses a $100 \mu\text{m}$ thick Kapton foil to reduce the neutron scattering from $\sim 20 \%$ to $\sim 5 \%$. For a Gd-GEM detector with low material budget readout, as used in the n_TOF measurements,

the detection efficiency at 2.4 \AA was simulated with Geant4 10.1 [19] to be around 15% with a threshold of 0 keV.

3 The experimental setup

The experimental setup at the n_TOF EAR2 beam line is shown in Figure 2a. The n_TOF experiment uses proton bunches that are first extracted from the PS accelerator, and subsequently hit a spallation target. Neutrons with energies between 10 meV and 1 GeV are delivered from the spallation target to the vertical EAR2 beam line, which has a neutron flight path of about 19 m. The NMX detector was installed at about 19.4 m from the center of the target on a support above the four n_TOF SiMON2 beam monitors. These beam monitors are installed around the beam pipe and detect tritons produced from the interaction of neutrons with the thin ^6LiF window inside the beam pipe. To measure separately the three different gadolinium regions, the detector was aligned in such a way that the beam was focused on one of the two samples or the natural Gd foil visible in Figure 2b. After taking data for a few hours, the neutron beam was stopped and the detector moved. At the position of the detector (1.17 m above the floor) we measured a beam size of about 24 mm FWHM in x direction and 26 mm FWHM in y direction. At a height of 1.6 m above the floor a beam width of 21 mm FWHM was measured by the n_TOF collaboration [20], we thus slightly overmeasure the width, probably by measuring part of the halo.

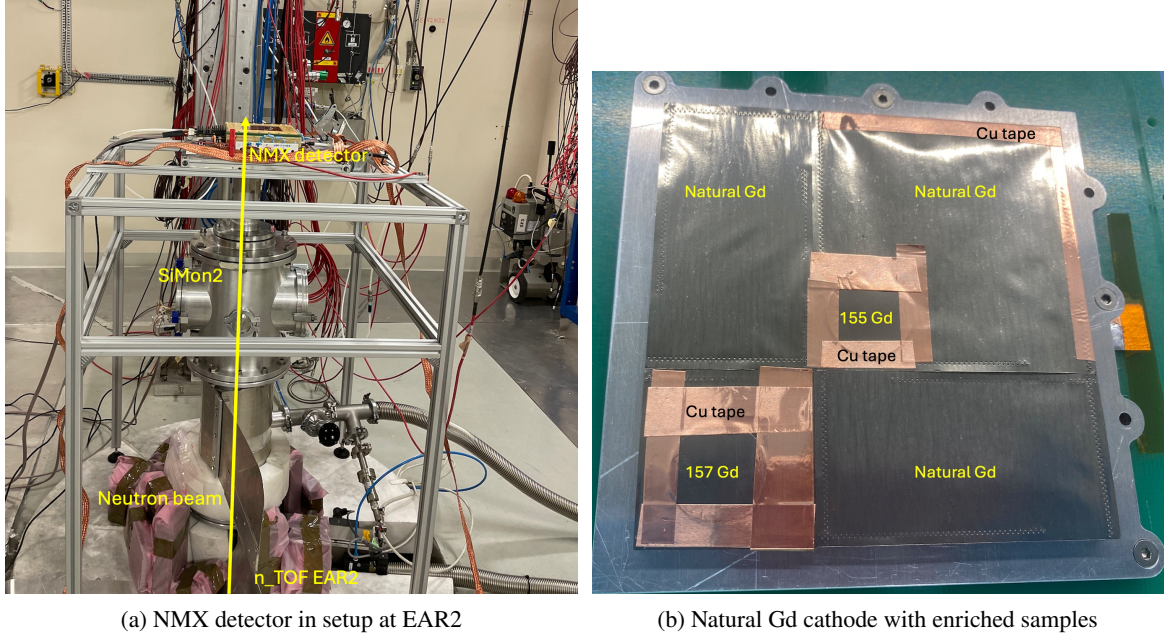


Figure 2. Detector setup in the experimental cave of EAR2. The neutron beams moves in the vertical direction from the floor to the ceiling (left). Two samples of enriched ^{155}Gd and ^{157}Gd were installed in the NMX detector on the natural Gd cathode (right).

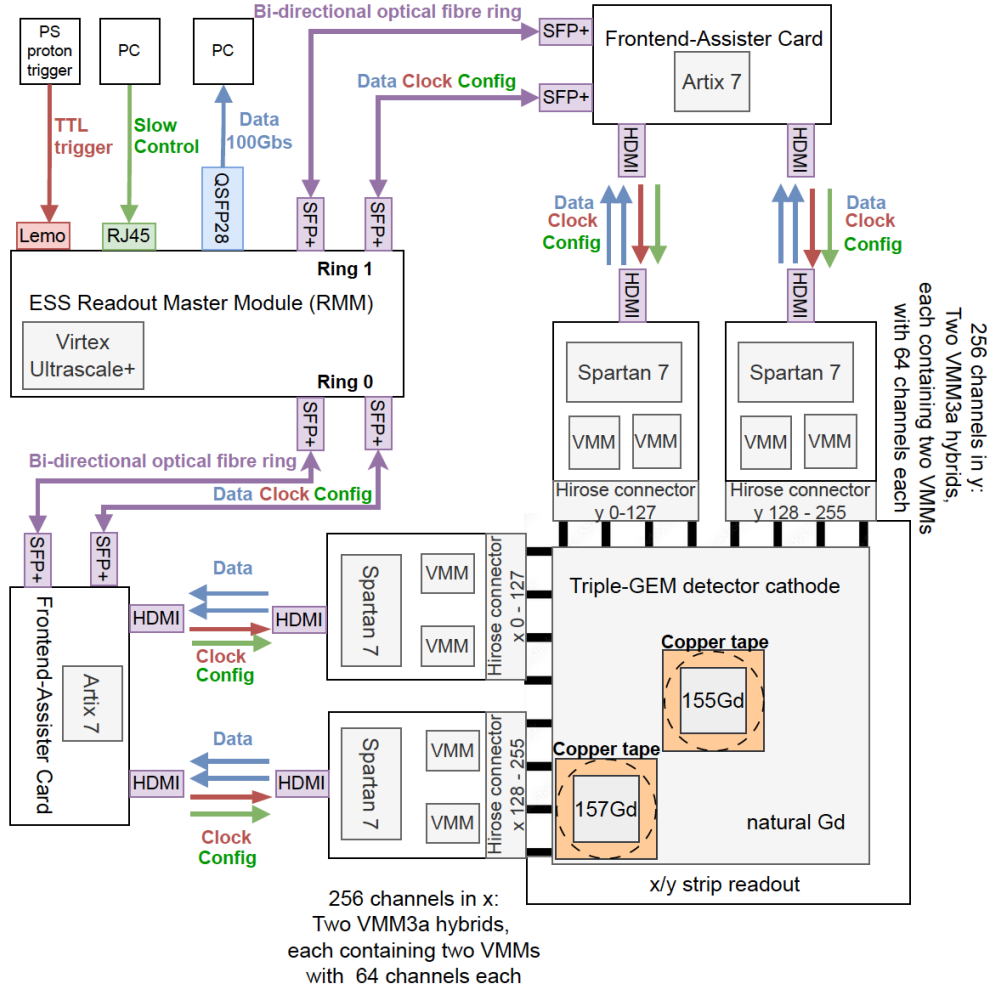


Figure 3. Schematic drawing of the detector and the readout system.

4 The ESS readout system

The measurements at the n_TOF EAR2 beam line at CERN described in this paper are the first time-of-flight experiment carried out with the NMX detector and the ESS readout system. A schematic drawing of the experimental setup is shown in figure 3. Two circular enriched Gd samples of 20 mm diameter with thicknesses of 40 μm (^{155}Gd) and 80 μm (^{157}Gd) were taped with Copper tape to the 25 μm thick cathode of natural Gd in such a way that a good electrical connection was made (figure 2b).

Two VMM3a hybrids were connected in x and y direction to the x/y strip readout of the detector. On each of the hybrids, the two VMM3a chips (64 channels per ASIC) digitize the electrical strip signals. The digitized signal is then transmitted to the Spartan 7 FPGA on the hybrid, which sends it 8b/10b encoded via LVDS over HDMI cable to the assister card. The assister cards serve as concentrators for the data from up to 6 hybrids. In the present experiment, two assister cards with two hybrids each were installed, one for the x- and one for the y- dimension. The assister

cards convert the electrical signals into optical signals and send the data 8b/10b encoded over a bi-directional fibre ring with 6.6 Gbps to the ESS Readout Master Module (RMM). The RMM supports up to 12 bi-directional rings, which can have up to 16 assister nodes each. To optimize the bandwidth, two rings with only one node each were used. The RMM again is a concentrator module, and combines the data from all 12 rings into UDP jumbo frames transmitted via 100 Gbps to the data acquisition PC. On the PC, the complete data is written to disk. A fraction of the events is visualized to ensure the correct operation of the detector and readout system.

The DAQ PC also contains the slow control software that is used to configure the RMM, the assister cards, and the VMM3a hybrids. The slow control information is sent via an 1 Gbps ethernet connection to the RMM, which then passes the relevant slow control information on to each assister node on the 12 rings. The assisters again send the relevant slow control information to the hybrids. The clock is distributed the same way down from the RMM via the assisters to the hybrids. The RMM has the possibility to use an external time reference, but for the n_TOF measurements the internal oscillator of the RMM was used. The PS proton trigger is fed into the TTL input of the RMM. The trigger signal appears then as trigger time stamp inside the readout data packages.

5 Time-of-flight measurements

During the measurement campaign in March 2024, the intensity of the proton bunches that hit the spallation target was close to the nominal intensity of $7\text{E}+12$ protons per bunch. At this intensity the neutron flux was too high for our detector, which was suffering from saturation effects.

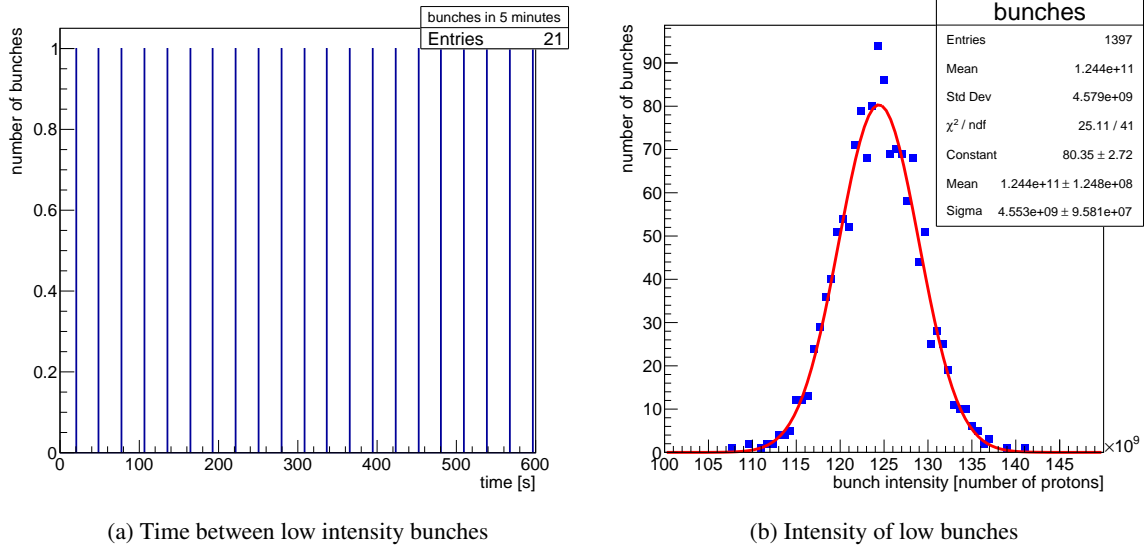


Figure 4. October 2024: Frequency and intensity of low intensity bunches (around $1.25\text{E}+11$ protons). If there are low intensity bunches between the high intensity bunches, they appear about every 30 s. Higher intensity bunches, and especially the full intensity bunches of more than $7.0\text{E}+12$ protons, produce too many neutrons for our detector and lead to saturation. Bunches with intensities larger than $2\text{E}+11$ protons have thus been excluded from our analysis. On average there was a protons bunch every 4s during our experiment in October.

In October 2024, however, in addition to the nominal intensity bunches, smaller bunches with an intensity of around 1.25×10^{11} protons were regularly injected into the PS. Whereas on average every 4 seconds a bunch of all intensities was hitting the target, the frequency of the low intensity bunches was much lower, with one bunch every 30 seconds, as shown in Figure 4a. To normalize our neutron intensity measurements, the proton intensity responsible for the neutron production has to be known. The time and the intensity of the extracted proton bunches was provided to us in the form of a root tree by the n_TOF experiment. We then matched the Unix time stamp in nanoseconds of the proton bunch to our proton trigger time stamp with 11.36 ns resolution. Since we were relying on the internal oscillator of the RMM as time reference, during the successful matching a time drift of 6 ns per second (6 ppm) was observed between our recorded trigger time stamp and the time stamp in the root tree.

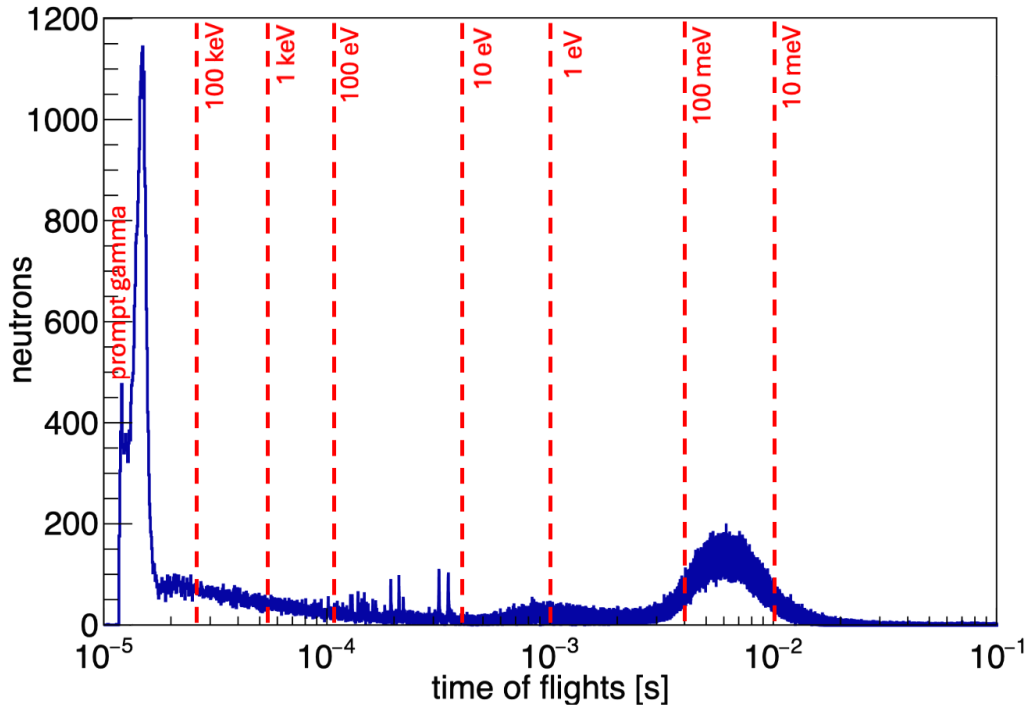


Figure 5. Time-of-flight measurements of neutrons detected on the enriched ^{157}Gd sample. On the left of the plot one can see the prompt gamma peak, which occurs at about 12 μs . The prompt gamma time-of-flight represents the t_0 for the calculation of the neutron energy.

In Figure 5 the time-of-flight of neutron events detected on the enriched ^{157}Gd sample is shown. The prompt gammas appear at about 12 μs . This t_0 time serves subsequently as time correction to convert the time-of-flight into energy. To convert the time-of-flight to energy, the following relativistic equations can be used:

$$\text{length flight path } l_{path} = 19.4 \text{ m} \quad (5.1)$$

$$\text{time correction } t_{cor} = 12 \mu s \quad (5.2)$$

$$\text{speed of light } c = 299792458 \frac{m}{s} \quad (5.3)$$

$$\text{neutron mass } m = 939.56542052 \cdot 10^6 \frac{eV}{c^2} \quad (5.4)$$

$$\gamma = \frac{1}{\sqrt{1 - \left(\frac{l_{path}}{(tof - t_{cor}) \cdot c}\right)^2}} \quad (5.5)$$

$$\text{relativistic kinetic energy } E_{kin} = (\gamma - 1) \cdot m \cdot c^2 \text{ eV} \quad (5.6)$$

$$(5.7)$$

For neutrons with energies below a few keV, the non-relativistic equations suffice:

$$\text{kinetic energy } E_{kin} = \frac{1}{2} \frac{m}{c^2} v^2 \text{ eV} \quad (5.8)$$

$$= \frac{1}{2} \frac{m}{c^2} \left(\frac{l_{path}}{tof - t_{cor}}\right)^2 \text{ eV} \quad (5.9)$$

$$(5.10)$$

Two regions of the time-of-flight spectrum will be analyzed in more detail, the resonant region and the thermal neutron peak. The region with neutron energies between 1 eV and 200 eV shows numerous resonant peaks that can be clearly distinguished in the ADC distribution of the VMM3a channels displayed in figure 6.

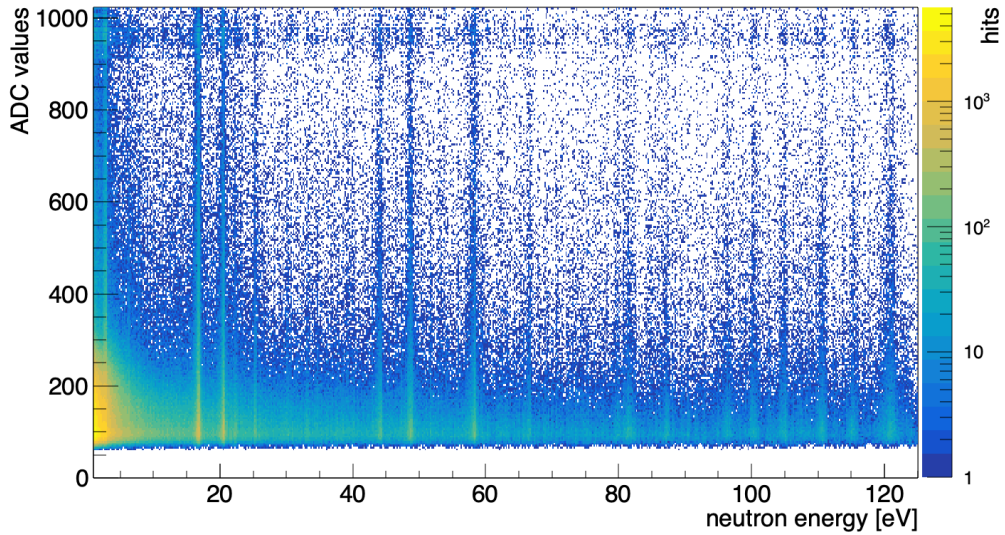


Figure 6. Resonant peaks between 1 eV and 125 eV visible in the ADC distribution measured with ^{157}Gd .

When using 19.4 m as flight path and 12 μs as time correction, the measured peaks do not perfectly overlap with the cross section peaks of ^{157}Gd . To find the exact time correction and flight path that makes the peaks overlap, two peaks in the ENDF VIII.0 ^{157}Gd cross section plot (figure 7) were chosen. Their time-of-flight and energy was subsequently put into the following system of equations, which is then solved for t_{cor} and l_{path} .

$$E_{kin} = \frac{1}{2} \frac{m}{c^2} v^2 \text{ eV} \quad (5.11)$$

$$= \frac{1}{2} \frac{m}{c^2} \left(\frac{l_{path}}{tof - t_{cor}} \right)^2 \text{ eV} \quad (5.12)$$

$$l_{path} = (tof_1 - t_{cor}) \cdot \sqrt{\frac{2E_1}{m}} \cdot c \quad (5.13)$$

$$= (tof_2 - t_{cor}) \cdot \sqrt{\frac{2E_2}{m}} \cdot c \quad (5.14)$$

$$K_1 = \sqrt{\frac{2E_2}{m}} \cdot c \quad (5.15)$$

$$K_2 = \sqrt{\frac{2E_1}{m}} \cdot c \quad (5.16)$$

$$t_{cor} = \frac{tof_2 \cdot K_2 - tof_1 \cdot K_1}{K_2 - K_1} \quad (5.17)$$

$$(5.18)$$

The results for four different pairs of peaks are shown in table 1 below.

Peak1 Energy	Peak 1 ToF	Peak2 Energy	Peak 2 ToF	t_{cor}	l_{path}
16.77 eV	350.3 μs	120.90 eV	137.8 μs	11.7 μs	19.18 m
16.77 eV	350.3 μs	137.90 eV	129.9 μs	11.8 μs	19.17 m
16.77 eV	350.3 μs	143.55 eV	127.5 μs	11.7 μs	19.18 m
16.77 eV	350.3 μs	239.32 eV	101.5 μs	11.9 μs	19.17 m

Table 1. Calculated t_{cor} and l_{path} from energy and time-of-flight of cross-section peaks.

Whereas the calculated time correction t_{cor} agrees with the measured value of the prompt gamma flash, the calculated flight path of 19.18 m is about 1.1% shorter than the assumed distance of 19.4 m. The resonance energies measured by the n_TOF collaboration [10] differ with e.g. $E_1=16.7946 \text{ eV}$ and $E_2=120.861 \text{ eV}$ from the ENDF VIII.0 values. Using the n_TOF collaboration values, one arrives at $t_{cor}= 11.35 \mu\text{s}$, and $l_{path}=19.21 \text{ m}$. More precisely, the calculated flight path l_{path} actually consists of the geometrical distance L_0 and an energy dependent part, the moderation length λ . For the purpose of this paper, and when looking at energy ranges between 1eV and 200 eV, it suffices to use a λ that is constant in this range.

Figure 7 uses the re-calculated l_{path} and t_{cor} . It shows in the energy range between 1eV and 125 eV the ENDF VIII.0 total neutron cross sections [21] for ^{157}Gd and ^{155}Gd . The measured data were obtained by converting the time-of-flight of each VMM3a channel into an energy for the run when the neutron beam was focused on the ^{157}Gd . As expected, the measured peaks agree with the

large ^{157}Gd cross section peaks. The ^{157}Gd measurement lasted only 10 hours, and due to detector saturation only 833 bunches with an average intensity of $1.24\text{E}+11$ protons could be included in the analysis. Therefore not enough statistics were acquired to find agreement with the smaller ^{157}Gd cross section peaks. On the other hand, for very high ^{155}Gd cross section peaks, one also sees small peaks in the measured ^{157}Gd data. There are two reasons for this. First, the analyzed region does not exclusively consist of ^{157}Gd , but also includes on the outside away from the center of the beam a few mm^2 of natural Gd. Second, the sample of enriched ^{157}Gd contains a 0.29 % contamination of ^{155}Gd [10].

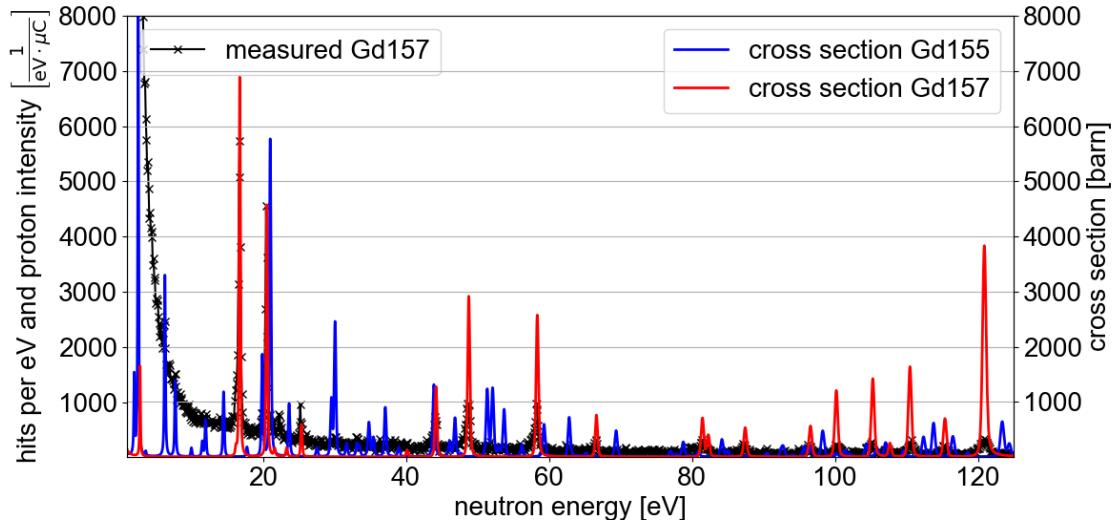


Figure 7. Hit distribution per eV normalized with the proton current as measured on the ^{157}Gd sample. On the second y-axis at the right side the ENDF VIII.0 total neutron cross sections for ^{157}Gd and ^{155}Gd can be seen.

Figure 8 compares the ENDF VIII.0 cross sections with the data measured on the different Gd regions. As expected the measured resonances for ^{157}Gd follow the ^{157}Gd ENDF VIII.0 resonances, and the measured ^{155}Gd resonances agree with the ^{155}Gd ENDF VIII.0 peaks. The strong resonance in the ^{157}Gd ENDF VIII.0 at 16.77 eV is also weakly seen in the measured ^{155}Gd data. As in the case of the ^{157}Gd sample, the analyzed region for ^{155}Gd also contains at the outside, away from the center of the beam, several mm^2 of natural Gd. Further, the ^{155}Gd sample is contaminated with 1.14 % of ^{157}Gd . The measured resonances in the natural Gd region follow both the ^{155}Gd and the ^{157}Gd ENDF VIII.0 resonances, but with reduced amplitudes compared to the enriched samples.

6 Comparison of the efficiencies of ^{157}Gd , ^{155}Gd and natural Gd

The NMX instrument at ESS will use thermal and cold neutrons between 1.8 and 10 Å. At n_TOF, the largest neutron intensity was measured between 0.8 and 2.0 Å in the thermal region, as shown in Figure 9. For each of the different Gd samples (^{155}Gd and ^{157}Gd) and the natural Gd cathode, data was taken with the beam focused on the sample. For the ^{155}Gd and ^{157}Gd samples, one can see a square region in the center, since copper tape was used to attach the samples to the natural Gd

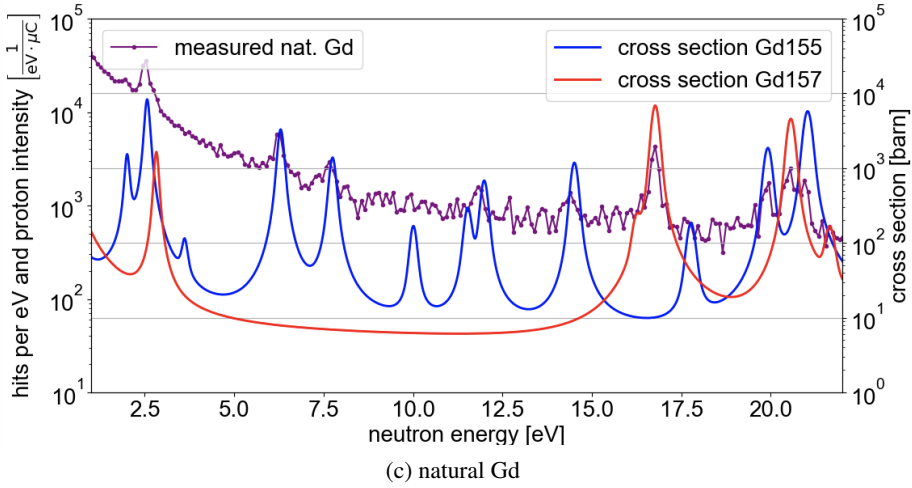
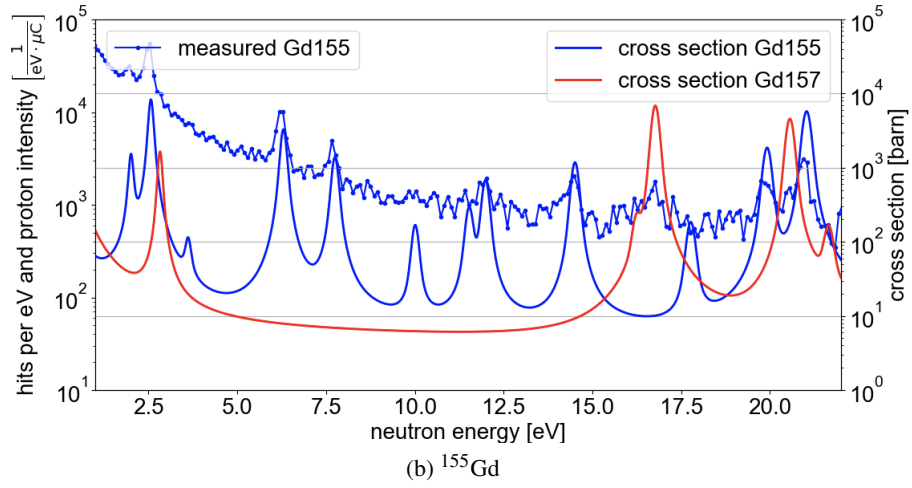
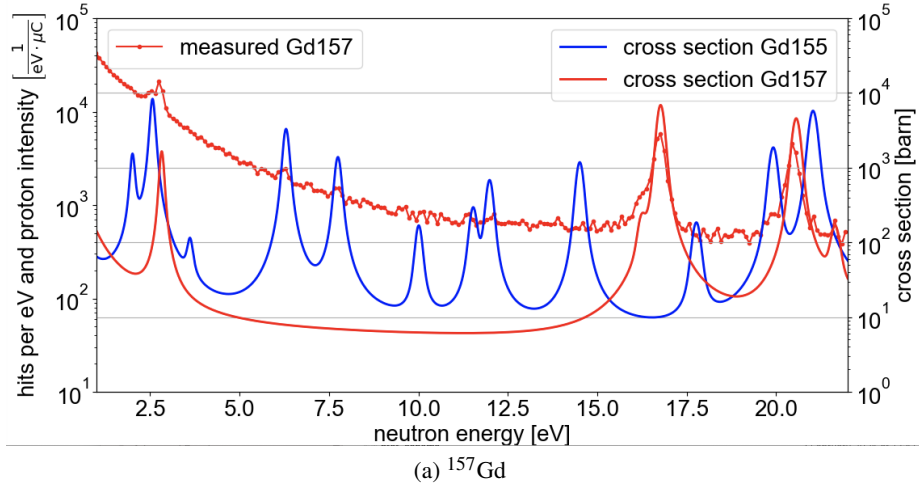


Figure 8.

cathode. On the natural Gd cathode the beam profile is rounder. Using the time-of-flight method, the number of counts for wavelengths between 0.75 Å and 1.85 Å was determined in bins of 0.1 Å. As displayed in figure 10, a Gaussian fit was used to find the center of the beam. A region of 16 x 16 pixels (+/- 8 pixels around the center of the fit) was defined to compare the measured intensity for different wavelengths and different Gd isotopes.

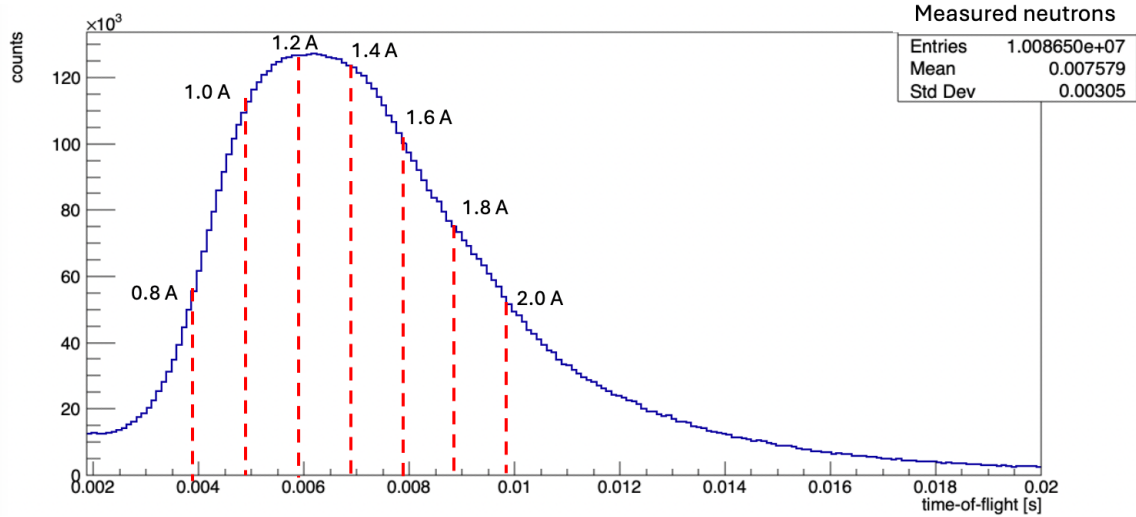


Figure 9. Thermal neutron peak as measured with the ^{157}Gd sample. The largest intensity was measured in the wavelength range between 0.8 Å and 2.0 Å.

Due to the lack of an absolute efficiency reference, only the relative efficiencies of ^{157}Gd and ^{155}Gd compared to natural Gd can be plotted. Figure 11 shows the n_TOF measurements ^{155}Gd (green) and ^{157}Gd (red) ratios relative to natural Gd. Bruckner et. al. studied in 1999 at the ILL in Grenoble the neutron detection efficiency of Silicon detectors with a natural Gd converter and an enriched ^{157}Gd converter. The efficiency ratio that was derived from their article [22] is shown in blue. D. A. Abdushukurov published in 2013 mathematical calculations and simulations of the neutron detection efficiency in [23]. The ratio between ^{157}Gd and natural Gd that was calculated from his results is displayed in purple. Whereas the simulations predict an efficiency about twice as high for ^{157}Gd compared to natural Gd at 1.8 Å, the measurements show smaller gains. The solid state detector data from ILL shows an improvement of 80%, and at n_TOF with the Gd-GEM detector an improvement of 60% was measured. Bruckner et al. also observed that the absolute measured efficiency of ^{157}Gd was higher than the simulated one, hypothesizing that the difference can be explained by the additional detection of gamma background.

Due to the much higher neutron capture cross-section of ^{157}Gd , naturally more neutrons are detected with ^{157}Gd . However, the gamma sensitivity of the detector is independent of the converter material. The larger the contribution of gammas to the total count rate, the smaller the relative gain when exchanging a natural Gd converter with an enriched ^{157}Gd converter. For the particular setup with the Gd-GEM detector at n_TOF, another explanation could be the focusing of the beam onto the enriched samples. Whereas the natural Gd cathode was large enough to see the full beam profile, the enriched samples only had an area of about 1 cm x 1 cm. The beam was not properly focused on the center of these squares, and part of the highest intensity regions were on the copper

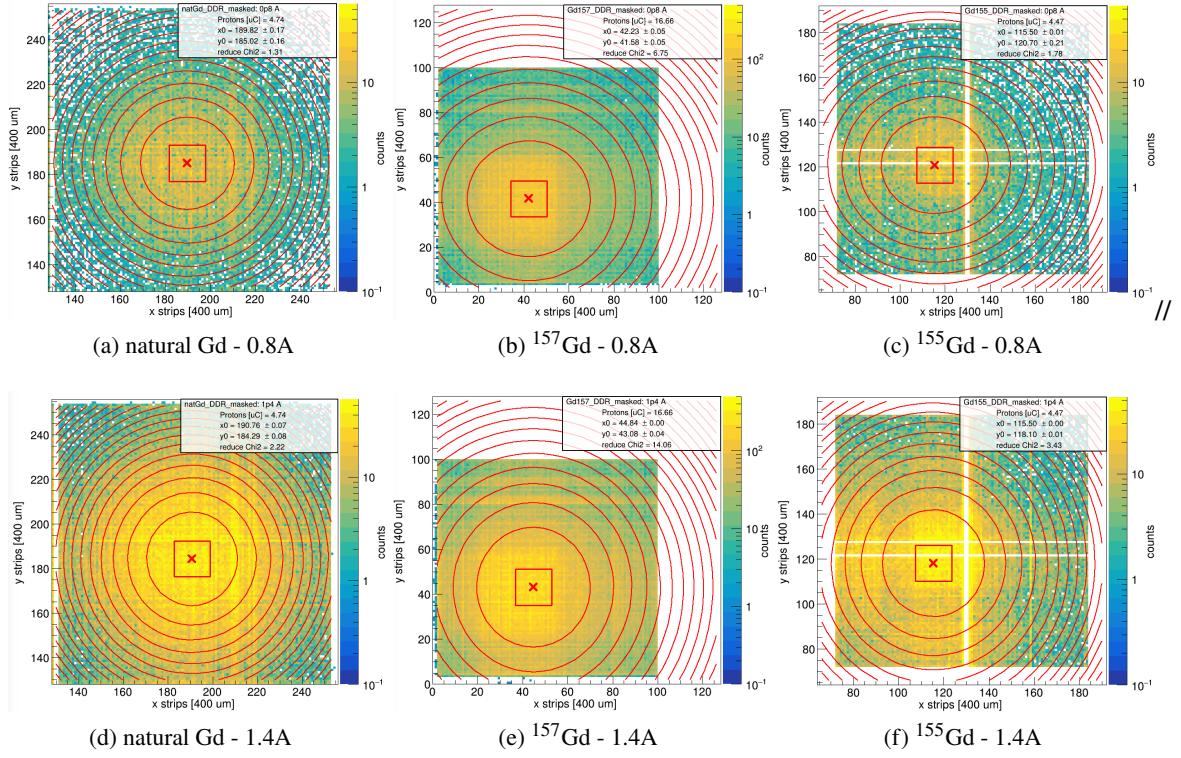


Figure 10. Comparison of neutron beam spots on the three different Gd samples at 0.8 Å and 1.4 Å. For the ^{157}Gd and ^{155}Gd samples, one can see a square region in the center, and the copper tape that was used to attach the samples to the natural Gd cathode. The red square of ± 8 pixels around the center of the fit shows the 16 x 16 pixel zone that was considered for the intensity comparison between the different Gd isotopes.

tape. For ^{157}Gd the highest intensity as determined by the fit is shifted from the center of the square to the right side, as visible in figure 10. The beam was even more offset when measuring the ^{155}Gd sample, with the highest intensity in the lower left corner of the sample.

The highest count rates on the VMM3a ASICs were measured between 1.0 and 1.4 Å in the ^{157}Gd region. In this wavelength range the number of hits per VMM3a remains at an instantaneous rate of more than 8 million hits per second. The maximum instantaneous hit rate measured amounts to 8.6 MHz, almost reaching the absolute theoretical VMM3a hit rate limit of 8.8 MHz [16]. As shown in 12, for natural Gd the maximum rate stays below the rate limit with a maximum of 8 MHz for 1.2 Å neutrons. It is thus probable that saturation effects artificially limited the count rate during the ^{157}Gd measurement, whereas for natural Gd the count rate stayed below the technical limits. This would explain the dip in the red curve in figure 11 in this wavelength area. For the ^{155}Gd the maximum hit rate stays well below any limit, but the measurements suffered from damaged readout strips in the center of the detector, where the sample was located. These defective strips are visible as white lines.

Taken together, gamma background detection, bad focusing, saturation effects and defective readout strips contributed to measuring for the enriched Gd samples a smaller relative gain increase than expected from simulations. Therefore the efficiency increase of 60% if using an enriched

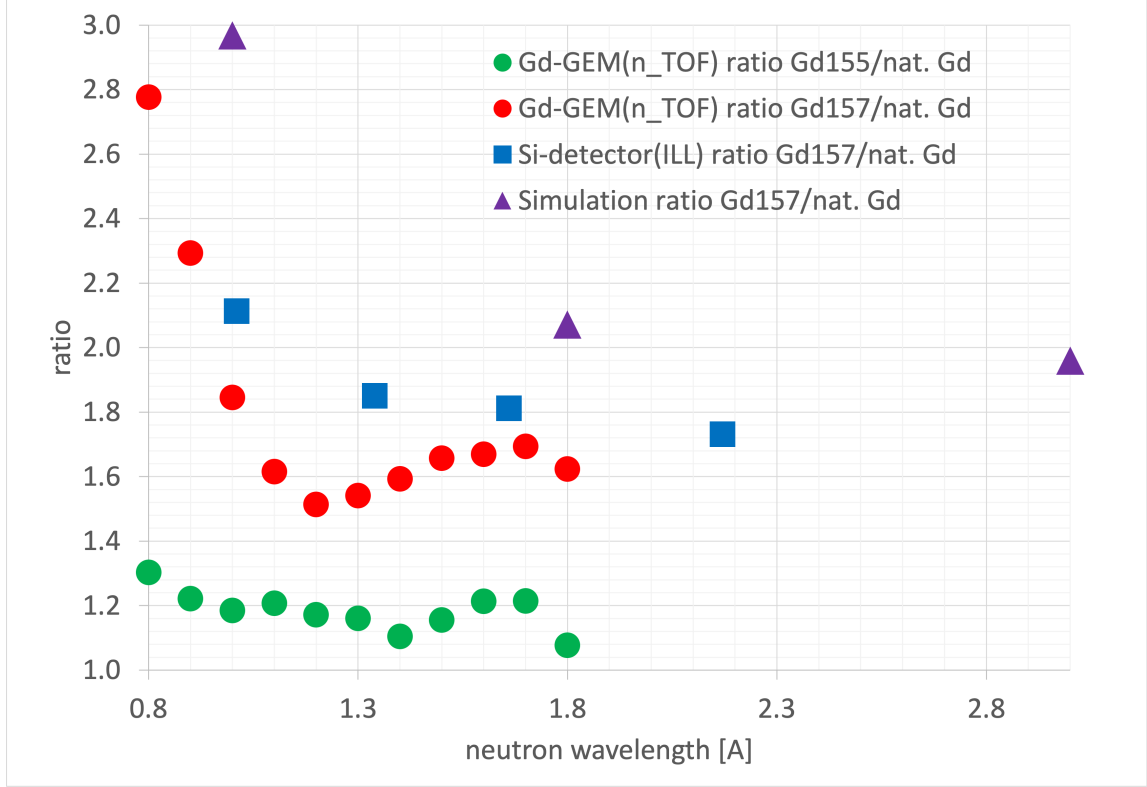


Figure 11. Relative efficiency ratios between ^{157}Gd and natural Gd and ^{155}Gd and natural Gd. Whereas simulations predicted for ^{157}Gd 100% more efficiency compared to natural Gd at 1.8 Å, earlier measurements at ILL with a solid state detector resulted in an 80 % improvement. With the Gd-GEM at n_TOF about 60 % more efficiency was measured.

^{157}Gd converter should be seen as lower threshold of the possible efficiency gain.

7 Conclusion

The measurements presented in this paper are the first successful time-of-flight measurements with the NMX detector prototype and the ESS VMM readout. A $10 \times 10 \text{ cm}^2$ prototype of the NMX detector was equipped with two enriched Gd samples (^{157}Gd and ^{155}Gd) that were attached with copper tape to the natural Gd cathode of the detector. Three sets of measurements were taken, with the beam focused on either the natural Gd, or the ^{157}Gd and ^{155}Gd samples. Using the time-of-flight technique with the subsequent conversion of time-of-flight into energy, the resonant region between 1 eV and 200 eV of the ^{157}Gd and ^{155}Gd cross sections was studied. The peaks in the resonant region were clearly visible as having higher ADC values in the ADC spectrum. Additionally the resonant peaks had a larger number of counts per energy bin. Comparing the count rate at the center of the beam for natural Gd, ^{157}Gd and ^{155}Gd , the enriched ^{157}Gd showed a efficiency that was between 180 % and 60 % larger in the thermal energy region for wavelengths between 0.8 Å and 1.8 Å. The measured 60 % increase in efficiency is smaller than expected from simulations (100 %) and previous measurements with solid state detectors (80 %). Gamma background detection, bad

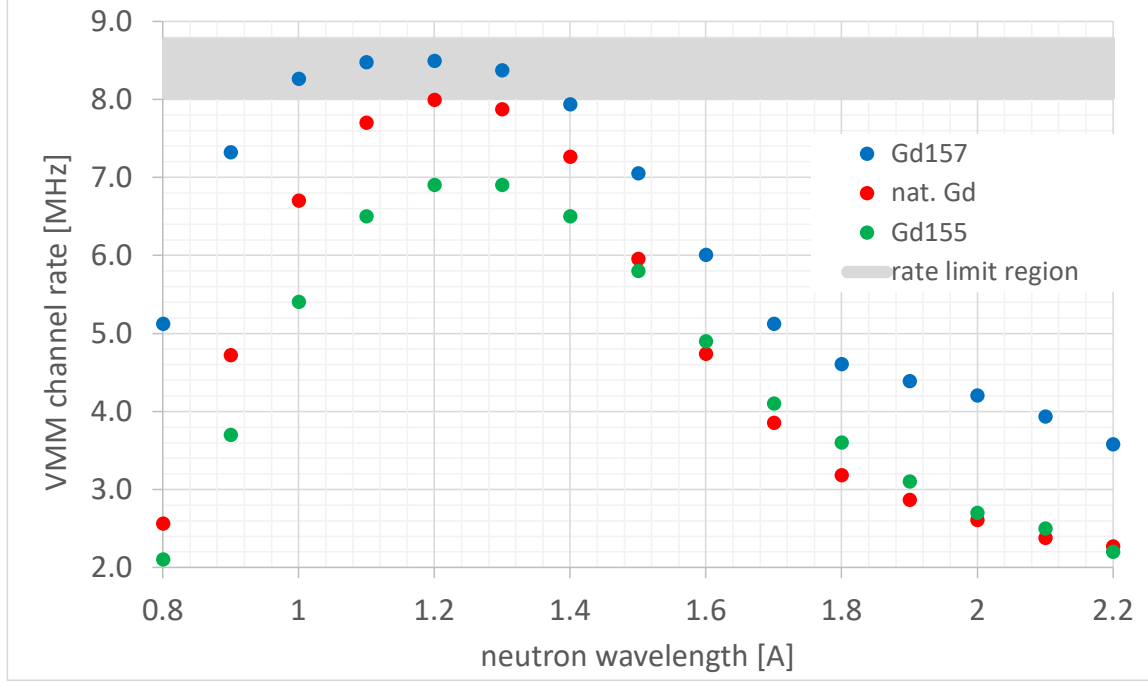


Figure 12. The theoretical absolute rate limit for one VMM3a ASIC (on the RD51 hybrid) is 8.8 MHz. At rates above 8 MHz, as reached for the VMM3a ASICs in the ^{157}Gd region, saturation effects and thus data loss can occur.

focusing and saturation effects explain these deviations. The upgrade of the natural Gd converter to enriched ^{157}Gd would thus lead to an efficiency increase of at least 60 %. To decide whether the upgrade to enriched ^{157}Gd is economically feasible, one has to study whether the savings in beam time exceed the cost of the upgrade itself.

Acknowledgments

The authors would like to acknowledge and thank the n_TOF collaboration for lending the enriched Gd samples to ESS, and allocating beam time to us. In particular we would like to thank Alberto Mengoni, Riccardo Mucciola and Francisco Garcia Infantes for all their support during the test beams and with the interpretation of our data.

References

- [1] “European spallation source ess eric.” [Online]. Available: <http://europeanspallationsource.se/>
- [2] S. Peggs *et al.*, “Ess technical design report,” European Spallation Source ERIC, Tech. Rep. ESS-2013-0001, 2013.
- [3] K. H. Andersen *et al.*, “The instrument suite of the european spallation source,” *Nuclear Instruments and Methods in Physics Research A*, vol. 957, p. 163402, 2020. [Online]. Available: <https://doi.org/10.1016/j.nima.2020.163402>
- [4] O. Kirstein *et al.*, “Neutron position sensitive detectors for the ess,” in *Proceedings of the The 23rd International Workshop on Vertex Detectors (VERTEX2014)*, vol. 227, September 2014, pp. 15–19.
- [5] M. Markó, G. Nagy, G. Aprigliano, and E. Oksanen, “Chapter seven - neutron macromolecular crystallography at the european spallation source,” *Methods in Enzymology*, vol. 634, pp. 125–151, 2020.
- [6] M. Titov and L. Ropelewski, “Micro-pattern gaseous detector technologies and rd51 collaboration,” *Modern Physics Letters A*, vol. 28, p. 1340022, 2013.
- [7] F. M. B. Guerard, R. Hall-Wilton, “Prospects in mpgds development for neutron detection,” *CERN Document Server CDS*, 2013, summary based on presentations during RD51 Academia-Industry Matching Event CERN October 2013, RD51-NOTE-2014-003. [Online]. Available: <https://cds.cern.ch/record/2119706>
- [8] C. Altunbas, “Construction, test and commissioning of the triple-gem tracking detector for compass,” *Nuclear Instruments and Methods in Physics Research A*, vol. 490, pp. 177–203, 2002.
- [9] F. Sauli, “Gem: A new concept for electron amplification in gas detectors,” *Nuclear Instruments and Methods in Physics Research A*, vol. 386, pp. 531–534, 1997.
- [10] M. Mastromarco *et al.*, “Cross section measurements of $^{155,157}\text{Gd}(n,\gamma)$ induced by thermal and epithermal neutrons,” *The European Physical Journal A*, vol. 55, no. 1, p. 9, 2019. [Online]. Available: <https://doi.org/10.1140/epja/i2019-12692-7>
- [11] D. Pfeiffer *et al.*, “The utpc method: improving the position resolution of neutron detectors based on mpgds,” *Journal of Instrumentation*, vol. 10, no. 04, p. P04004, 2015. [Online]. Available: <http://stacks.iop.org/1748-0221/10/i=04/a=P04004>
- [12] D. Pfeiffer, F. Resnati, J. Birch, M. Etxegarai, R. Hall-Wilton, C. Höglund, L. Hultman, I. Llamas-Jansa, E. Oliveri, E. Oksanen, L. Robinson, L. Ropelewski, S. Schmidt, C. Strelti, and P. Thuiner, “First measurements with new high-resolution gadolinium-gem neutron detectors,” *Journal of Instrumentation*, vol. 11, no. 05, p. P05011, 2016.
- [13] G. D. Geronimo *et al.*, “Vmm1 - an asic for micropattern detectors,” in *2012 IEEE Nuclear Science Symposium and Medical Imaging Conference Record (NSS/MIC)*, 2012, pp. 633–639.
- [14] G. Iakovidis, “Vmm3a, an asic for tracking detectors,” *Journal of Physics: Conference Series*, vol. 1498, p. 012051, 2020.
- [15] M. Lupberger *et al.*, “Implementation of the vmm asic in the scalable readout system,” *Nuclear Instruments and Methods in Physics Research A*, vol. 903, pp. 91–98, 2018.
- [16] D. Pfeiffer *et al.*, “Rate-capability of the vmm3a front-end in the rd51 scalable readout system,” *Nuclear Instruments and Methods in Physics Research Section A: Accelerators, Spectrometers, Detectors and Associated Equipment*, vol. 1031, p. 166548, 2022. [Online]. Available: <https://www.sciencedirect.com/science/article/pii/S016890022200153X>

- [17] “Ifé.” [Online]. Available: <http://ife.no/>
- [18] A. Bressan *et al.*, “Two-dimensional readout of gem detectors,” *Nuclear Instruments and Methods in Physics Research A*, vol. 425, pp. 254–261, 1999.
- [19] S. Agostinelli, J. Allison, K. Amako, J. Apostolakis, H. Araujo, P. Arce, M. Asai, D. Axen, S. Banerjee, G. Barrant, F. Behner, L. Bellagamba, J. Boudreau, L. Broglia, A. Brunengo, H. Burkhardt, S. Chauvie, J. Chuma, R. Chytrcek, G. Cooperman, G. Cosmo, P. Degtyarenko, A. Dell’Acqua, G. Depaola, D. Dietrich, R. Enami, A. Feliciello, C. Ferguson, H. Fesefeldt, G. Folger, F. Foppiano, A. Forti, S. Garelli, S. Giani, R. Giannitrapani, D. Gibin, J. G. Cadenas, I. González, G. G. Abril, G. Greeniaus, W. Greiner, V. Grichine, A. Grossheim, S. Guatelli, P. Gumplinger, R. Hamatsu, K. Hashimoto, H. Hasui, A. Heikkinen, A. Howard, V. Ivanchenko, A. Johnson, F. Jones, J. Kallenbach, N. Kanaya, M. Kawabata, Y. Kawabata, M. Kawaguti, S. Kelner, P. Kent, A. Kimura, T. Kodama, R. Kokoulin, M. Kossov, H. Kurashige, E. Lamanna, T. Lampén, V. Lara, V. Lefebure, F. Lei, M. Liendl, W. Lockman, F. Longo, S. Magni, M. Maire, E. Medernach, K. Minamimoto, P. M. de Freitas, Y. Morita, K. Murakami, M. Nagamatsu, R. Nartallo, P. Nieminen, T. Nishimura, K. Ohtsubo, M. Okamura, S. O’Neale, Y. Oohata, K. Paech, J. Perl, A. Pfeiffer, M. Pia, F. Ranjard, A. Rybin, S. Sadilov, E. D. Salvo, G. Santin, T. Sasaki, N. Savvas, Y. Sawada, S. Scherer, S. Sei, V. Sirotenko, D. Smith, N. Starkov, H. Stoecker, J. Sulkimo, M. Takahata, S. Tanaka, E. Tcherniaev, E. S. Tehrani, M. Tropeano, P. Truscott, H. Uno, L. Urban, P. Urban, M. Verderi, A. Walkden, W. Wander, H. Weber, J. Wellisch, T. Wenaus, D. Williams, D. Wright, T. Yamada, H. Yoshida, and D. Zschesche, “Geant4 - a simulation toolkit,” *Nuclear Instruments and Methods in Physics Research A*, vol. 506, no. 506, pp. 250–303, 2003.
- [20] C. Weiß *et al.*, “The new vertical neutron beam line at the cern n_tof facility design and outlook on the performance,” *Nuclear Instruments and Methods in Physics Research Section A: Accelerators, Spectrometers, Detectors and Associated Equipment*, vol. 799, pp. 90–98, 2015. [Online]. Available: <https://www.sciencedirect.com/science/article/pii/S0168900215008566>
- [21] “Evaluated nuclear data file (endf).” [Online]. Available: <https://www-nds.iaea.org/exfor/endf.htm>
- [22] G. B. *et al.*, “Position sensitive detection of thermal neutrons with solid state detectors (gd si planar detectors),” *Nuclear Instruments and Methods in Physics Research A*, vol. 424, pp. 183–189, 1999.
- [23] D. A. Abdushukurov, “Mathematical modeling of the efficiency gadolinium based neutron converters,” *Applied Mathematics*, vol. 4, no. 8A, pp. 27–33, 2013.